J. Fluid Mech. (2001), *vol.* 430, *pp.* 361–380. Printed in the United Kingdom

The difference in turbulent diffusion between active and passive scalars in stable thermal stratification

By KOUJI NAGATA AND SATORU KOMORI

Department of Mechanical Engineering, Kyoto University,
Kyoto 606-8501, Japan

(Received 5 May 1999 and in revised form 27 September 2000)

The difference in turbulent diffusion between active scalar (heat) and passive scalar (mass) in a stable thermally stratified flow is investigated both experimentally and numerically. The experiments are conducted in an unsheared thermally stratified water flow downstream of a turbulence-generating grid. Passive mass is released into the stable thermally stratified flow from a point source located 60 mm downstream from the grid. Instantaneous streamwise and vertical velocities, the temperature of the active scalar and the concentration of the passive scalar are simultaneously measured using a combined technique with a two-component laser-Doppler velocimeter (LDV), a resistance thermometer and a laser-induced fluorescence (LIF) method. From the measurements, turbulent heat and mass fluxes and eddy diffusivities for both active heat and passive mass are estimated. To investigate the Prandtl or Schmidt number effects on the difference in turbulent diffusion between active heat and passive mass, a three-dimensional direct numerical simulation (DNS) based on a finite difference method is applied to stable thermally stratified flows of both water and air behind the turbulence grid. The Schmidt number of passive mass in the DNS is set to the same value as the Prandtl number of active heat.

The results show that stable stratificaion causes a large difference in eddy diffusivities between active heat and passive mass. The numerical predictions by the DNS are in qualitative agreement with the measurements despite the assumption of the same molecular diffusivity for active heat and passive mass. The difference suggests that the assumption of identical eddy diffusivity for active heat and passive mass, used in conventional turbulence models, gives significant errors in estimating heat and mass transfer in a plume under stably stratified conditions.

1. Introduction

Owing to increasing interest in recent environmental problems, much attention has been paid to the heat and mass transfer mechanism in environmental flows. Flows in the ocean and atmospheric boundary layer are often density stratified and the diffusion of scalar such as heat and mass is strongly affected by buoyancy. It is, therefore, of great importance to investigate the buoyancy effects on heat and mass transfer in predicting the turbulent diffusion of scalar quantities in the environment. Besides the environmental problems, practical problems such as the designing of industrial heat and mass transfer equipment involve complicated phenomena due to the buoyancy effects and the elucidation of these buoyancy effects is required.

For engineering purposes, time-averaged transport equations for heat and mass:

$$\frac{\partial \bar{T}}{\partial t} + \overline{U_j}\frac{\partial \bar{T}}{\partial x_j} = \frac{\partial}{\partial x_j}\left(\alpha\frac{\partial \bar{T}}{\partial x_j} - \overline{u_j\theta}\right), \tag{1.1}$$

$$\frac{\partial \bar{C}}{\partial t} + \overline{U_j}\frac{\partial \bar{C}}{\partial x_j} = \frac{\partial}{\partial x_j}\left(\mathscr{D}\frac{\partial \bar{C}}{\partial x_j} - \overline{u_jc}\right), \tag{1.2}$$

are solved to obtain the local time-averaged temperature and concentration. Here $\bar{T}$ and $\bar{C}$ are the time-averaged temperature and concentration, $\overline{U_j}$ the time-averaged velocity in the j-direction, α the thermal diffusivity, $\mathscr{D}$ the molecular diffusivity of mass, and $\overline{u_j\theta}$ and $\overline{u_jc}$ the turbulent heat and mass fluxes, respectively. To numerically solve the above equations, the turbulent heat and mass fluxes in (1.1) and (1.2) should be modelled. In the conventional gradient-diffusion models the vertical turbulent heat and mass fluxes in a thermally stratified flow are given by

$$\overline{v\theta} = -K_H\frac{\partial \bar{T}}{\partial y}, \tag{1.3}$$

$$\overline{vc} = -K_S\frac{\partial \bar{C}}{\partial y}, \tag{1.4}$$

where $v = u_2$ is the velocity fluctuation in the vertical y-direction. The basic assumption in the gradient-diffusion models is that the turbulent heat and mass fluxes are proportional to the local gradients of mean temperature and concentration. The eddy diffusivities for active heat and passive mass, K_H and K_S, have been assumed to be identical in stably stratified conditions (e.g. Yamada & Mellor 1975; Freeman 1977). Recent measurements by Komori & Nagata (1996) support this assumption in a stably stratified flow with identical initial and boundary conditions for active heat and passive mass. However, Warhaft (1976) predicted a difference in eddy diffusivities for active (heat) and passive (moisture) scalars by using the second-order closure model. For different initial and boundary conditions, Pearson, Puttock & Hunt (1983) and Hunt (1985) predicted a large difference in the eddy diffusivities for active heat and passive mass by using a statistical theory for the diffusion of passive scalar in a stably stratified flow. Kaltenbach, Gerz & Schumann (1994) performed a large-eddy simulation (LES) of a stratified flow with a Prandtl number $Pr = 2$ where passive scalar having the same molecular diffusivity as active heat (Schmidt number $Sc = 2$) is simultaneously diffused, and they found a large difference in the eddy diffusivities for active and passive scalars especially at the initial stage of diffusion. However, the conventional Smagorinsky model used for the subgrid diffusion of active and passive scalars is controversial since the interaction between active and passive scalars at the subgrid scale was less understood in the model. Of course, no experiment has been carried out to verify the difference in eddy diffusivities. Thus, the difference in eddy diffusivities for active heat and passive mass in strong stratification needs to be elucidated by a precise laboratory experiment or a direct numerical simulation (DNS).

The purpose of this study is to investigate the difference in turbulent diffusion between active heat and passive mass in a stable thermally stratified flow. Measurements were conducted using a combined technique with a two-component laser-Doppler velocimeter (LDV), a resistance thermometer and a laser-induced fluorescence (LIF) method (Komori & Nagata 1996). In order to investigate the effects of molecular diffusion on the difference in turbulent diffusion between active and passive scalars,

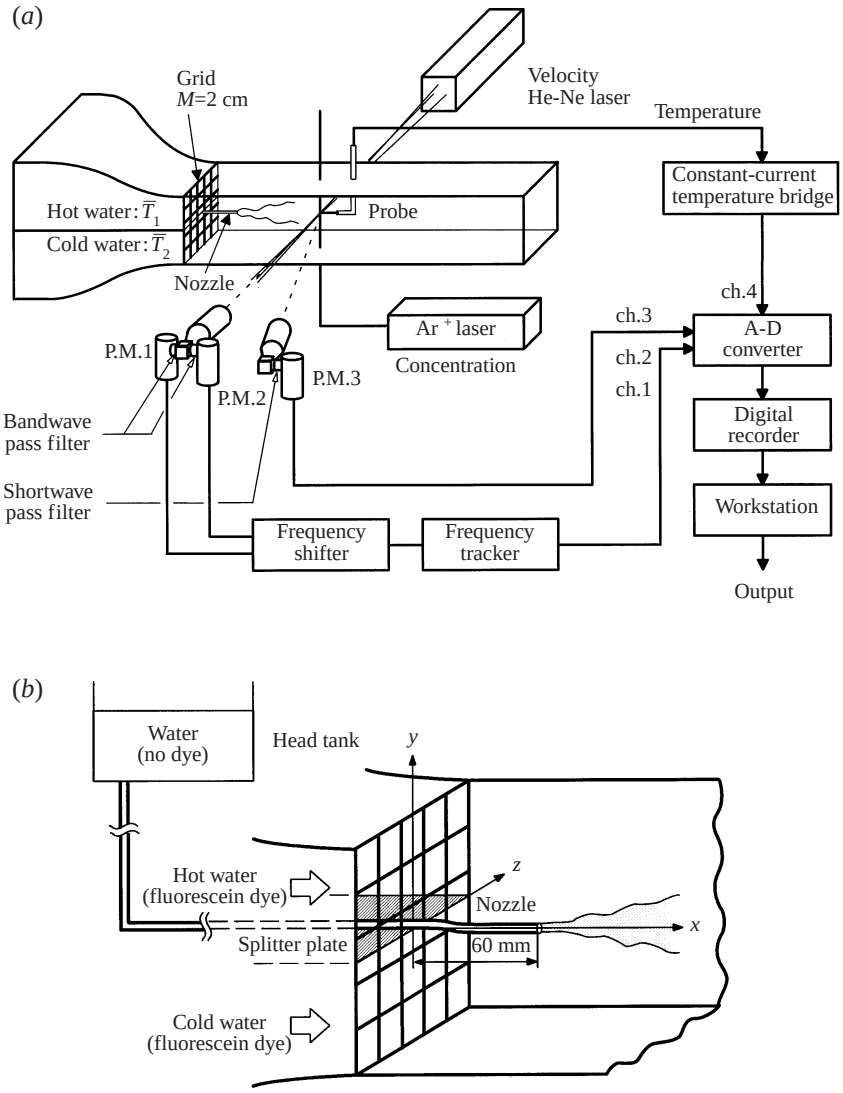

FIGURE 1. Experimental setup. (*a*) Measuring system and test apparatus. (*b*) Injection nozzle and coordinate system.

a three-dimensional direct numerical simulation (DNS) was applied to the stable thermally stratified flow.

2. Experiments

Figure 1(*a*) shows the measuring system and test apparatus. The test apparatus used was a water tunnel made of polymethylemethacrylate (PMMA), 1 m in length and 0.1×0.1 m in cross-section. A turbulence-generating grid was installed at the entrance to the test section, of round-rod, square-mesh, single-biplane construction. The mesh size M and diameter of the rod d were 2.0×10^{-2} m and 3.0×10^{-3} m, respectively.

A stable thermally stratified water flow was generated in the test section downstream

Run no.	Pr	Sc	$U_{av}(\mathrm{m\,s^{-1}})$	Re_M	Ri_b
E-I	5.0 (water)	600	0.125	2500	0
E-II	5.0 (water)	600	0.125	2500	7.8×10^{-3}
E-III	5.0 (water)	600	0.125	2500	3.9×10^{-2}
S-I	5.0 (water)	5.0	0.125	2500	0
S-II	5.0 (water)	5.0	0.125	2500	7.8×10^{-3}
S-III	5.0 (water)	5.0	0.125	2500	3.9×10^{-2}
S-IV	0.7 (air)	0.7	1.875	2500	0
S-V	0.7 (air)	0.7	1.875	2500	3.9×10^{-2}

TABLE 1. Experimental and numerical conditions.

of the turbulence-generating grid. Hot and cold water were separately pumped up from two big storage tanks to two head tanks, and then passed through the contraction, separated by a splitter plate into upper and lower sections. The high-temperature water in the upper stream was heated by a boiler and the temperature was regulated to a constant value in the storage tank by an electric heater connected to a thermometer. Thus, stable thermal stratification with an initial step temperature profile was formed behind the grid. The water (passive mass) was released as a plume from an injection nozzle located on the centreline at $y = 0$ and $z = 0$ and 60 mm downstream from the grid ($x/M = 3$) as shown in figure 1(b). The outside and inside diameters of the nozzle were 6 mm and 5 mm, respectively, and the water (passive mass) was poured into the nozzle from a head tank. The initial velocity of the plume was set to 1.12 times that of the ambient mean flow to maintain an isokinetic release based on the outside diameter of the nozzle (Gad-el-Hak & Morton 1979; Nakamura, Sakai & Miyata 1987). To minimize the buoyancy effects, the initial temperature of the plume was set to the mean temperature at $x/M = 3$ and $y = z = 0$. To enable us to determine the instantaneous concentration of the passive mass in the plume, sodium fluorescein dye ($C_{20}H_{10}Na_2O_5$) was homogeneously premixed in the ambient flow (in both the upper and lower streams) with the initial concentration of $5.0 \times 10^{-5}\,\mathrm{mol\,m^{-3}}$. Note that the plume has an apparent passive mass. In this case, the concentration of passive scalar in the plume released from the nozzle, normalized by the initial concentration C_0, was obtained by subtracting the normalized concentration of the sodium fluorescein dye in the ambient flow from unity. Three stratified conditions, namely neutral (Run E-I), weak (Run E-II) and strong (Run E-III) stratifications (for run conditions, see table 1), were used and the initial temperature difference between the upper and lower streams, $\Delta\bar{T} = \overline{T_1} - \overline{T_2}$, corresponded to 0 K, 3 K and 15 K, respectively. Mean velocities of the upper and lower streams, $\overline{U_1}$ and $\overline{U_2}$, were set to the same value of $0.125\,\mathrm{m\,s^{-1}}$. The Reynolds number based on the mesh size, $Re_M(= U_{av}M/\nu)$, was 2500 for all cases, where U_{av} is the cross-sectionally averaged velocity. The integral scale L and microscale λ at $x/M = 6$, deduced from the decay of $\overline{q^2}$ for neutrally stratified case, were 2.8 mm and 2.4 mm, respectively. The details of the flow field were shown in Komori & Nagata (1996).

Instantaneous velocity, temperature and concentration were simultaneously measured using a combined measuring technique as shown in figure 1(a) (Komori & Nagata 1996; Nagata & Komori 2000). The measuring technique combined a two-component laser-Doppler velocimeter with a resistance thermometer and a laser-induced fluorescence method. The laser-Doppler velocimeter used here was a DAN-

TEC 55X Modular system with a polarization beam splitter (55X24), a 40 MHz Bragg cell and a beam expander, and the laser was a 5 mW He-Ne laser with a 632.8 nm wavelength (Spectra Physics model 106-1). For temperature measurements, a cold-film I-probe of 10 μm diameter (TSI 1260-10W) operated by a constant-current temperature bridge (DANTEC 55M) was used, and it was located just behind the measuring point of velocity and concentration. The gap of about $\lambda = 0.5$ mm between velocity and temperature measuring points was compensated by giving a time lag of $\lambda/\bar{U}$ (=0.004 s) to the time records of the instantaneous temperature. For concentration measurements, a laser-induced fluorescence method was used, and the sodium fluorescein dye diffusing in the flow was illuminated by a high-power single-line mode argon-ion (Ar^+) laser of 0.8 W power and a 488 nm wavelength (LEXEL model 95-4). The He-Ne laser beams for velocity measurements were shone from the sidewall of the test section, and a single beam of an Ar^+ laser for concentration measurements was shone from the bottom wall. Both beams were focused by convex lenses and intersected perpendicularly at the same measuring point. The fluorescence from the measuring point was collected using an optical system (DANTEC 55X34). The focused and magnified fluorescence passed through a pinhole of 0.1 mm diameter, and it was received by a photomultiplier (HAMAMATSU R-777). The Doppler signals for velocity measurements were collected by another optical system (DANTEC 55X34) connected to two photomultipliers (DANTEC 55X08). The wavelength difference between Doppler signals from the scattered particles and fluorescence from the sodium fluorescein dye was about 100 nm and therefore the two lights were separated by installing optical filters between the optical system and photomultiplier. Shortwave and bandwave pass filters were installed in front of the photomultipliers for the concentration and velocity measurements, respectively. The details of the spectra of fluorescence and scattered lights, and transmittances of the optical filters are described in Komori *et al.* (1993*b*). The accuracy of the present combined technique, including the effects of the refractive index fluctuations on the measurements using LDV and LIF, was fully discussed in Komori & Nagata (1996).

The sampling interval and sample size were 2.5×10^{-4} s and 2.4×10^5, respectively, and they were enough to get reliable statistics. Statistical processing of the digitized data was done using a computer (SUN SPARC station).

3. Direct numerical simulation

In the experiments described above, the molecular diffusivities for active heat and passive mass are so different ($Pr = 5$ for active heat and $Sc \approx 600$ for passive mass) that the molecular diffusion may affect the difference in turbulent diffusion (eddy diffusivities) (Komori & Nagata 1996). To clarify the effects, a direct numerical simulation based on a finite difference method was applied to stable thermally stratified water and air flows downstream of the turbulence grid.

Figure 2 shows the schematic diagram of the computational domain. The computational domain was $640 \times 80 \times 80$ mm ($32M \times 4M \times 4M$) in the streamwise, vertical and spanwise directions. A square turbulence-generating grid, on which the velocity components are set to zero, was located 2.0×10^{-2} m downstream from the entrance. The mesh size M and thickness of the square rod d were 2.0×10^{-2} and 2.0×10^{-3} m, respectively. Unfortunately, the round-rod grid with a diameter of $d = 3.0 \times 10^{-3}$ m used in the experiments could not be used in the DNS because of the limitation of the coordinate system and computer memory. This prevented us from making quantitative comparison between the measurements and simulations. In addition, for

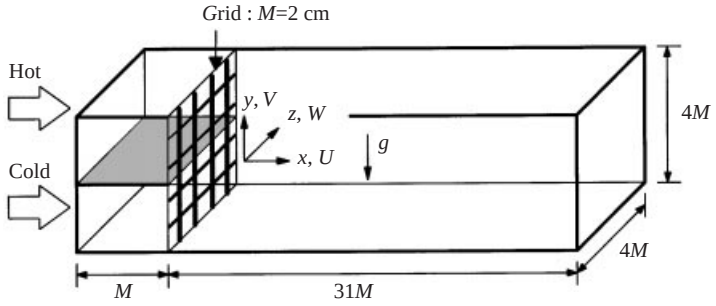

FIGURE 2. Computational domain for the DNS.

the same reason only four mesh points were used to describe the rod (cross-section). However, a typical grid-generated flow was generated in the DNS (Komori 1996; Nagata & Komori 1996) as shown later and we could successfully investigate the effects of Pr and Sc on the difference in turbulent diffusion. The numbers of grid points used here were $640 \times 160 \times 160$ in the streamwise, vertical and spanwise directions and therefore the grid spacings were 1.0×10^{-3} m in the streamwise direction and 5.0×10^{-4} m in the vertical and spanwise directions. The spatial resolution was comparable to the Kolmogorov scale of the flow. The slip conditions were adopted for the upper, lower and side boundaries since the computational domain was smaller than the experimental apparatus. Note that the turbulence is not generated by the wall but by the turbulence grid in the present flow. A test computation with the no-slip conditions for all the boundaries has shown that the results were almost the same in the central region. This implies that the presence of the walls does not alter the turbulence and scalar transport mechanism in the present flow.

The flow conditions are listed in table 1 together with the experimental conditions. The computations were conducted for water flows ($Pr = 5.0$) with the bulk Richardson numbers,

$$Ri_b = \frac{\beta g \Delta \bar{T} M}{U_{av}^2}, \tag{3.1}$$

of 0 (Run S-I), 7.8×10^{-3} (Run S-II) and 3.9×10^{-2} (Run S-III) (corresponded to the initial temperature differences of 0 K, 3 K and 15 K, respectively). Here β is the thermal volumetric expansion coefficient. Computations for air flows ($Pr = 0.7$) were added to investigate the difference in turbulent diffusion between active and passive scalars in stratified air flows (Runs S-IV and S-V). Hot and cold fluid was provided separately in the upper and lower streams upstream of the turbulence-generating grid (see figure 2). Thus, stable thermal stratification with an initial step temperature profile was generated behind the grid. Passive mass was released on the centreline ($y/M = z/M = 0$) at $x/M = 3$. To equate the molecular effects, the Schmidt number of the passive mass was set for all cases to the same value as the Prandtl number of the active heat. The Reynolds number based on the mesh size of the turbulence grid was 2500 for all cases.

The governing equations for an incompressible thermally stratified flow are

$$\frac{\partial U_i}{\partial x_i} = 0, \tag{3.2}$$

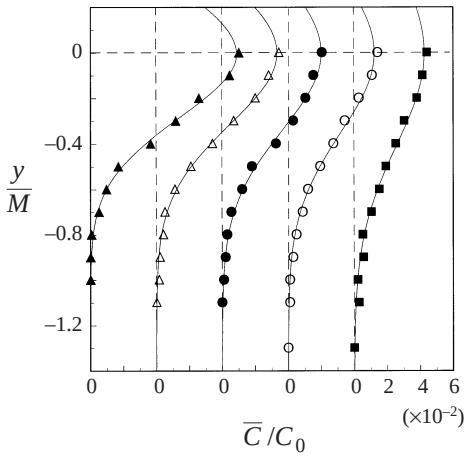

FIGURE 3. Vertical distributions of the mean concentration in a plume in the neutrally stratified flow: ▲, $x/M = 10$; △, $x/M = 12$; ●, $x/M = 14$; ○, $x/M = 16$; ■, $x/M = 18$.

$$\frac{\partial U_i}{\partial t} + U_j \frac{\partial U_i}{\partial x_j} = -\frac{\partial P}{\partial x_i} + \frac{1}{Re_M} \frac{\partial^2 U_i}{\partial x_j \partial x_j} + \delta_{2i} Ri_b T, \tag{3.3}$$

$$\frac{\partial T}{\partial t} + U_j \frac{\partial T}{\partial x_j} = \frac{1}{Re_M Pr} \frac{\partial^2 T}{\partial x_j \partial x_j}, \tag{3.4}$$

$$\frac{\partial C}{\partial t} + U_j \frac{\partial C}{\partial x_j} = \frac{1}{Re_M Sc} \frac{\partial^2 C}{\partial x_j \partial x_j}, \tag{3.5}$$

where all the quantities are non-dimensionalized by the grid mesh size M, cross-sectionally averaged velocity U_{av}, bulk-averaged density ρ_0, and initial temperature difference $\Delta\bar{T}$. Here, the Boussinesq approximation is adopted (Gerz, Schumann & Elghobashi 1989; Holt, Koseff & Ferziger 1992; Jacobitz, Sarkar & Van Atta 1997). The dimensionless parameters appearing in the governing equations are the Reynolds number $Re_M (= U_{av} M/\nu)$, the Prandtl number $Pr (= \nu/\alpha)$, the Schmidt number $Sc (= \nu/\mathscr{D})$ and the bulk Richardson number Ri_b.

The governing equations were discretized on a staggard mesh arrangement to construct a finite-difference formation. The nonlinear terms in the above Navier–Stokes (N–S) and transport equations for heat and mass were approximated by a fifth-order upwind scheme (Rai & Moin 1991; Komori *et al.* 1993*a*) and other spatial derivatives by a fourth-order central difference. The accuracy of the finite difference formulation was confirmed by Rai & Moin (1991) and Komori *et al.* (1993*a*). The HSMAC method was used to solve the N–S equations. The time integration of the N–S equations and transport equations for heat and mass was carried out by a second-order Runge–Kutta method. The full explicit approach used here requires smaller time steps, Δt, than an implicit formation to ensure numerical accuracy. Therefore, Δt was set to 6.4×10^{-4} s, which was much smaller than the Kolmogorov time scale. The computations were conducted by using a parallel super computer NEC SX-4.

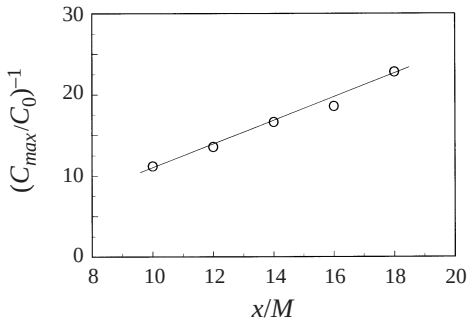

FIGURE 4. Streamwise variation of the reciprocal of the mean concentration on the plume axis.

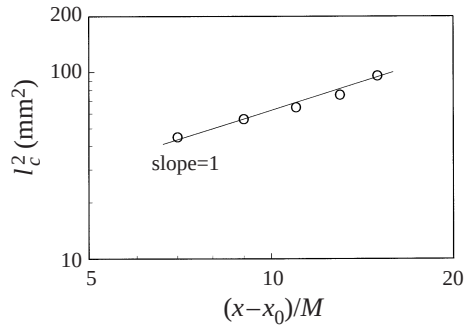

FIGURE 5. Streamwise variation of the square of the half-width of the mean concentration profile. x_0 is the virtual origin of the plume.

4. Experimental results and discussion

4.1. *Mean concentration profiles in a plume in neutral stratification*

To confirm the streamwise evolution of the mean concentration field, the mean concentration in a plume was measured at the locations $x/M = 10$, 12, 14, 16 and 18 in neutral stratification (Run E-I). The vertical distributions of the mean concentration are shown in figure 3. Here, the mean concentrations are normalized by the initial concentration, C_0. The peak values of the concentration on the plume axis (at $y/M = 0$) decrease in the downstream direction and the profiles become broad in the vertical direction with increasing x/M. This means that the passive mass released from the nozzle is diffused by the turbulent mixing. Figure 4 shows the streamwise distribution of the reciprocal of the mean concentration on the plume axis, C_{max}. The mean concentration on the plume axis follows well the hyperbolic decay law. Here, the hyperbolic decay law can be obtained from the transport equation for passive mass with no molecular diffusion term if we assume the similarity of mean concentration field (Nakamura *et al.* 1987). Figure 5 shows the streamwise distribution of the square of the half-width of the mean concentration profile. It can be seen that the variation of l_c^2 follows a 1-power law. Using these characteristic concentration and length, C_{max} and l_c, the mean concentration profiles are replotted in figure 6. The profile of the normalized mean concentration at each location has the shape described in terms of the following Gaussian function:

$$\frac{\bar{C}}{C_{max}} = \exp\left\{-(\ln 2)\left(\frac{y}{l_c}\right)^2\right\}. \tag{4.1}$$

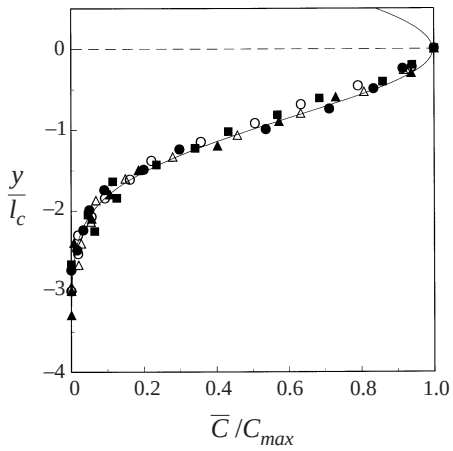

FIGURE 6. Vertical distribution of the normalized mean concentration. Symbols as in figure 3. The solid line shows the Gaussian curve (4.1).

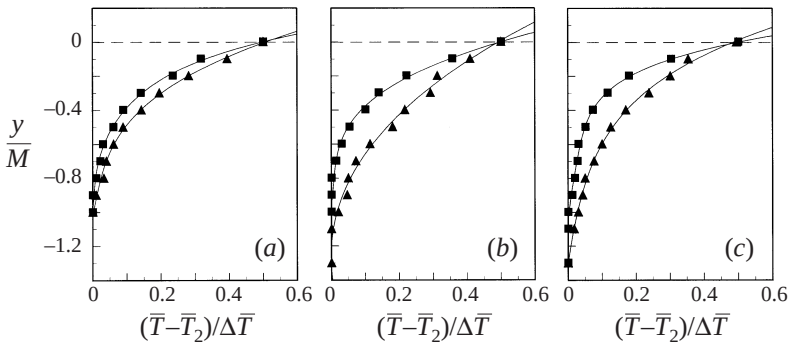

FIGURE 7. Vertical distributions of the mean temperature at (*a*) $x/M = 10$, (*b*) $x/M = 14$ and (*c*) $x/M = 18$: ▲, in the weakly stratified flow (Run E-II); ■, in the strongly stratified flow (Run E-III). The solid lines show the error functions for fitting the measurements. (For run conditions see table 1.)

The shape is in good agreement with that derived from the similarity analysis for the mean concentration field in neutral stratification. This suggests that a typical plume is formed in the test section in the region of $10 \leqslant x/M \leqslant 18$ and that the effects of disturbances from the inserted nozzle on the evolution of the plume are negligibly small.

4.2. *Effects of buoyancy on the mean temperature, mean concentration and vertical turbulent heat and mass fluxes*

Figure 7 shows the vertical distributions of the mean temperature at the locations $x/M = 10$, 14 and 18 in weak (Run E-II) and strong (Run E-III) stratifications. Here, the mean temperature is normalized by the initial temperature difference, $\Delta\bar{T} = \overline{T_1} - \overline{T_2}$. For both stratified cases, the profiles are approximated well by the error functions (Jayesh, Yoon & Warhaft 1991). In strong stratification, the mean temperature decreases rapidly in the downward direction compared to the weakly stratified case. This means that the strong stable stratification decreases the mixing layer thickness (Jayesh *et al.* 1991; Huq & Britter 1995). Figure 8 shows the vertical

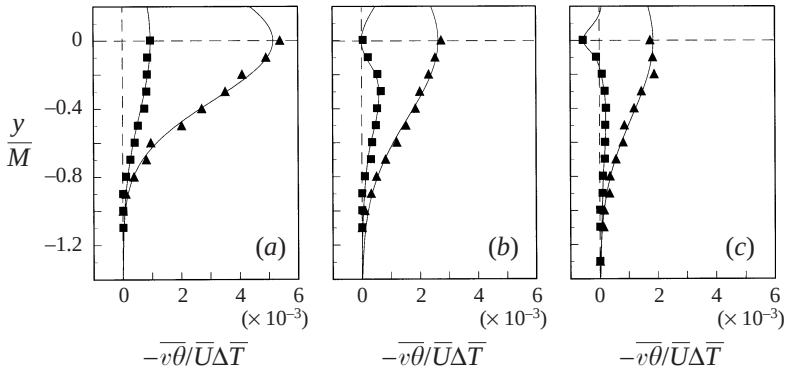

FIGURE 8. Vertical distributions of the normalized vertical heat flux at (*a*) $x/M = 10$, (*b*) $x/M = 14$ and (*c*) $x/M = 18$. Symbols as in figure 7.

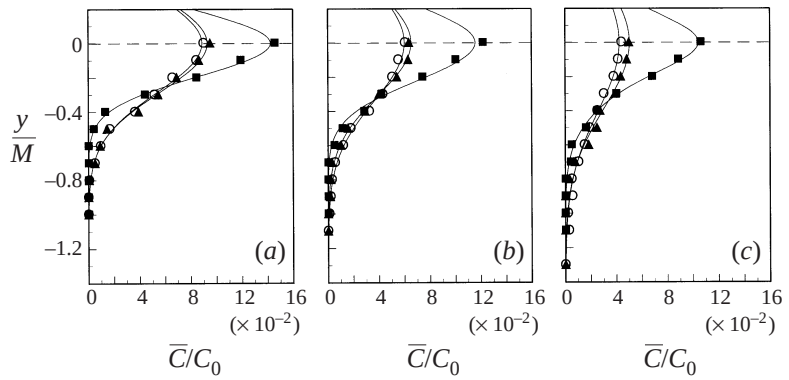

FIGURE 9. Vertical distributions of the mean concentration in a plume at (*a*) $x/M = 10$, (*b*) $x/M = 14$ and (*c*) $x/M = 18$: ○, in the neutrally stratified flow (Run E-I); ▲, in the weakly stratified flow (Run E-II); ■, in the strongly stratified flow (Run E-III).

distributions of the vertical heat flux under two stratified conditions, normalized by the product of the mean velocity, $\bar{U}$, and initial temperature difference, $\Delta\bar{T}$. The heat fluxes in strong stratification are remarkably suppressed by buoyancy and the heat flux at $x/M = 18$ indicates counter-gradient heat transfer (positive heat flux) in the central region of $|y/M| < 0.2$ where the temperature gradient is the largest. Counter-gradient transfer was first found in an open-channel flow by Komori *et al.* (1983). The effects of buoyancy on turbulence intensities, mean temperature and vertical turbulent heat flux are fully discussed in Komori & Nagata (1996).

Figure 9 shows the vertical distributions of the mean concentration in a plume at the locations $x/M = 10$, 14 and 18 in neutral (Run E-I), weak (Run E-II) and strong (Run E-III) stratifications. Here, the mean concentration is normalized by the initial concentration, C_0. It can be seen that the peak values of the concentration on the plume axis increase with increasing stability and the profiles become sharp. This means that the growth of the plume in the vertical direction is attenuated by stable stratification. The results are in qualitative agreement with previous measurements (Chaudhry & Meroney 1973; Britter *et al.* 1983). Figure 10 shows the vertical distributions of the vertical mass flux normalized by the product of $\bar{U}$ and C_0 under the three stratified conditions. The distributions indicate that the stable stratification

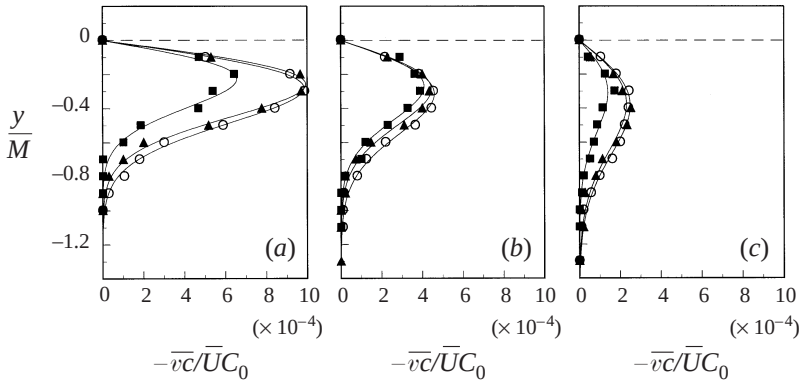

FIGURE 10. Vertical distributions of the normalized vertical mass flux at (*a*) $x/M = 10$, (*b*) $x/M = 14$ and (*c*) $x/M = 18$. Symbols as in figure 9.

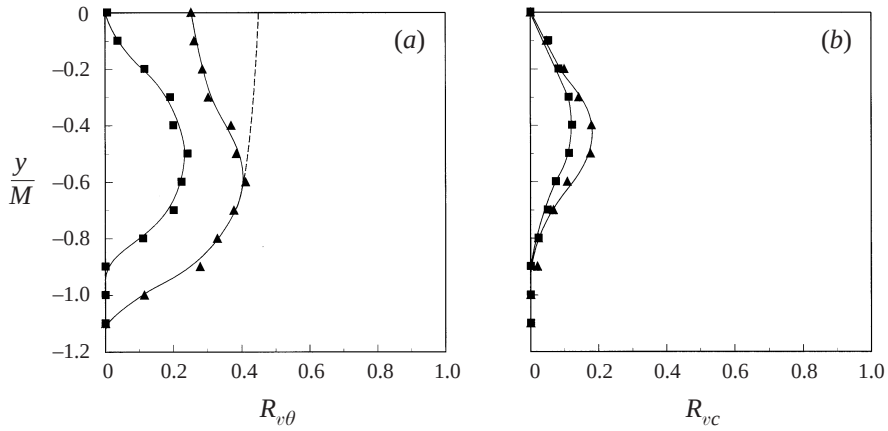

FIGURE 11. (*a*) Vertical distributions of the correlation coefficients between the vertical velocity and temperature fluctuations. Symbols as in figure 7. The dashed line shows the coefficient in the weakly stratified flow without a plume. (*b*) Vertical distributions of the correlation coefficients between the vertical velocity and concentration fluctuations. Symbols as in figure 7.

attenuates the vertical mass flux. For reference, vertical distributions of the correlation coefficients between the vertical velocity fluctuation and the scalar fluctuations are shown in figure 11. Here the profiles are obtained in weak and strong stratifications (Runs E-II and E-III) at $x/M = 14$. It can be seen that strong stable stratification weakens the correlation between the vertical velocity fluctuation and scalar fluctuations. It should be noted that the correlation coefficient between v and θ is reduced by the temperature contamination due to the plume upstream in the central region of $|y/M| < 0.6$ compared to the flow without the plume (dashed line in figure 11 for weak stratification), since the plume has the initial temperature $T = (\overline{T_1} + \overline{T_2})/2$.

4.3. *Eddy diffusivities for active scalar* (*heat*) *and passive scalar* (*mass*)

Eddy diffusivities for active heat and passive mass were estimated by (1.3) and (1.4). Figure 12 shows the vertical distributions of the eddy diffusivities for active heat and passive mass at the locations $x/M = 10$, 14 and 18 in neutral, weak and strong stratifications. The difference in the eddy diffusivities obviously exists even for the weakly stratified case. The stronger stratification causes a larger difference in the eddy

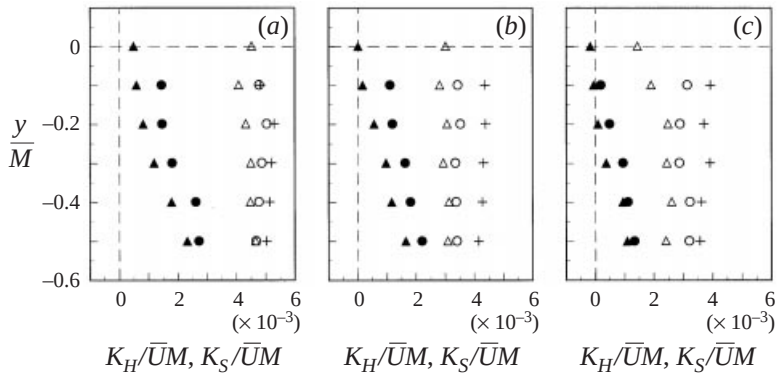

FIGURE 12. Vertical distributions of the eddy diffusivities for active heat and passive mass at (*a*) $x/M = 10$, (*b*) $x/M = 14$ and (*c*) $x/M = 18$: +, K_S in the neutrally stratified flow (Run E-I); △, K_H in the weakly stratified flow (Run E-II) ○, K_S in the weakly stratified flow (Run E-II); ▲, K_H in the strongly stratified flow (Run E-III); ●, K_S in the strongly stratified flow (Run E-III).

diffusivities between active heat and passive mass. The difference may be understood if we consider the transport equation for vertical heat and mass fluxes:

$$\frac{\mathrm{D}(-\overline{v\theta})}{\mathrm{D}t} = \overline{v^2}\frac{\partial \bar{T}}{\partial y} \underbrace{-\beta g\overline{\theta^2}}_{\text{buoyancy}} + (\alpha+\nu)\overline{\frac{\partial v}{\partial x_i}\frac{\partial \theta}{\partial x_i}} + \overline{\frac{p}{\rho_0}\frac{\partial \theta}{\partial y}} + \frac{\partial}{\partial x_i}\left[\overline{u_i v\theta} + \delta_{2i}\frac{\overline{p\theta}}{\rho_0}\right], \tag{4.2}$$

$$\frac{\mathrm{D}(-\overline{vc})}{\mathrm{D}t} = \overline{v^2}\frac{\partial \bar{C}}{\partial y} \underbrace{-\beta g\overline{c\theta}}_{\text{buoyancy}} + (\mathscr{D}+\nu)\overline{\frac{\partial v}{\partial x_i}\frac{\partial c}{\partial x_i}} + \overline{\frac{p}{\rho_0}\frac{\partial c}{\partial y}} + \frac{\partial}{\partial x_i}\left[\overline{u_i vc} + \delta_{2i}\frac{\overline{pc}}{\rho_0}\right], \tag{4.3}$$

where p is the pressure fluctuation and δ_{ij} is the Kronecker delta. The first term on the right-hand sides of (4.2) and (4.3) represents the mean production and the second term represents the buoyancy production (or destruction). The mean production terms will not cause the difference in the eddy diffusivities, since they are proportional to the mean temperature and concentration gradients. The dissipation and diffusion terms (the third and last terms on the right-hand sides of (4.2) and (4.3)) are also of less importance (Wyngaard, Coté & Izumi 1971). On the other hand, when the initial and boundary conditions for active heat and passive mass are very different (i.e. temperature and concentration fluctuation are initially uncorrelated), $\overline{\theta^2}$ and $\overline{c\theta}$ in the buoyancy terms have the relation

$$\overline{\theta^2} \gg \overline{c\theta}, \tag{4.4}$$

for short-time dispersion as shown in figure 13. This means that the turbulent diffusion of passive scalar is less affected by buoyancy than that of active scalar. Thus, we can understand that the difference in the buoyancy terms causes the difference in the eddy diffusivities. A conceptual illustration showing the different diffusion mechanisms is given in figure 14. (Note that the illustration is based on a Lagrangian framework although the measured turbulence quantities were Eularian.) Here it is interesting to refer to the Lagrangian energy analysis of Pearson *et al.* (1983). They developed a Lagrangian model to predict fluid element motions and vertical diffusion in a stably stratified flow. Their model showed how the fluid element paths eventually diverge from the path of a marked molecule released from a point source. For the present flow, we can easily understand how the paths of active scalar diverge from the paths

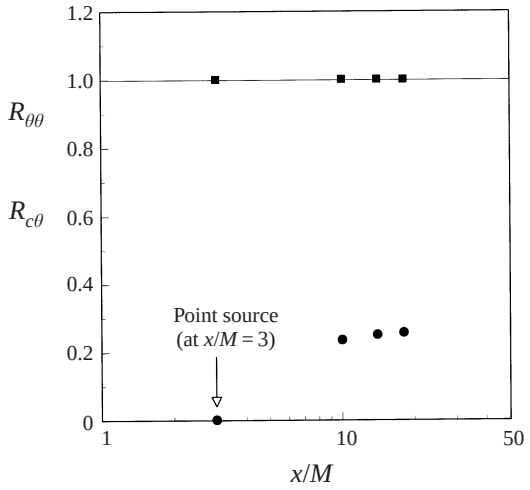

FIGURE 13. Streamwise variations of the correlation coefficient between temperature and concentration fluctuations in the strongly stratified flow (Run E-III): ■, $R_{\theta\theta}$; ●, $R_{c\theta}$.

of passive scalar, since the heat (active scalar) has a dynamical restoring force in a stably stratified flow.

5. Numerical results and discussion

5.1. *Mean concentration in a plume in neutral stratification*

Figure 15 shows the vertical distributions of the mean concentration in a plume at the locations $x/M = 10$, 12, 14, 16 and 18 in the neutrally stratified water flow (Run S-I). Here, the mean concentration and vertical distance are normalized by the mean concentration on the plume axis, C_{max}, and half-width of the mean concentration profile, l_c, respectively. The normalized mean concentration profiles have the Gaussian shape (4.1). For reference, streamwise variations of the reciprocal of C_{max} and the square of l_c are shown in figures 16 and 17, respectively. The distributions of C_{max} and l_c^2 follow well the hyperbolic decay law and a 1-power law. The normalized mean concentration profiles, together with the profiles of C_{max}^{-1} and l_c^2, suggest that a typical plume is formed in the DNS.

5.2. *Eddy diffusivities for active heat and passive mass in stable stratification*

Figures 18, 19, 20 and 21 show the vertical distributions of the mean temperature and concentration, vertical heat and mass fluxes at the locations $x/M = 10$, 14 and 18 under neutrally (Run S-I), weakly (Run S-II) and strongly (Run S-III) stratified conditions. The predictions are in qualitative agreement with the measurements. It can be seen that the vertical heat and mass transport is suppressed by buoyancy under the stably stratified conditions.

Figure 22 shows the vertical distributions of the eddy diffusivities for active heat and passive mass predicted under three stratified conditions. For the neutrally stratified case, K_S falls on the same line as K_H despite the different initial and boundary conditions between mean temperature and concentration. For the stably stratified cases, the difference in the eddy diffusivities is evident even in weak stratification and the difference becomes significant in strong stratification. Figure 23 shows the ratio of the computed eddy diffusivity for active heat to that for passive mass against the local

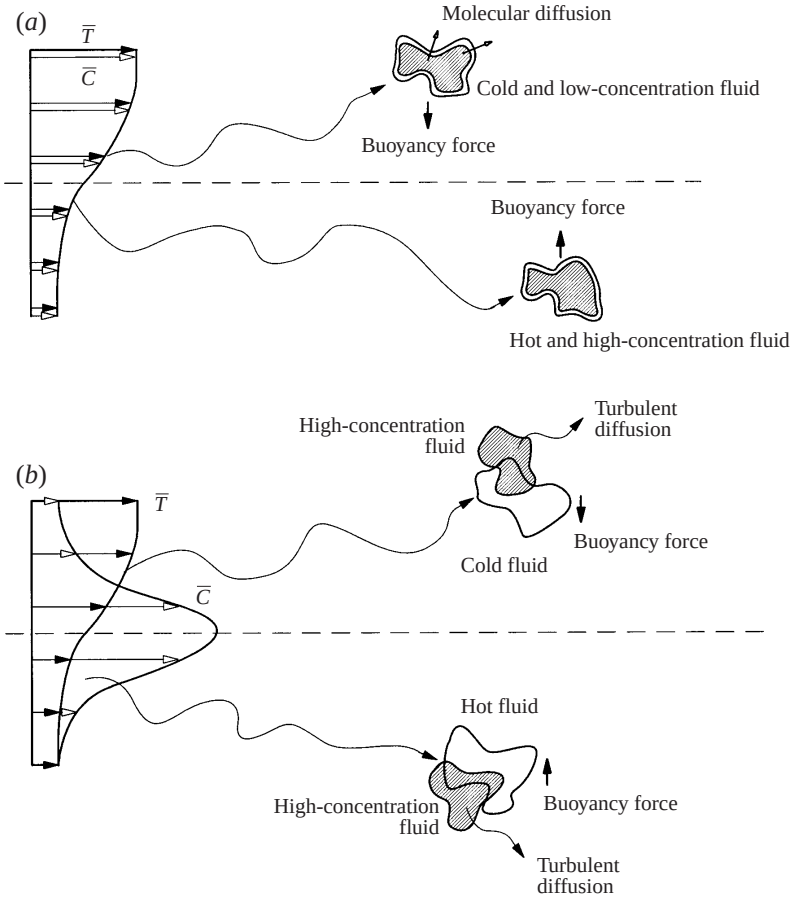

FIGURE 14. Turbulent diffusion mechanism of active heat and passive mass. (*a*) Identical initial and boundary conditions for active heat and passive mass (Komori & Nagata 1996): buoyancy affects turbulent diffusions of both active heat and passive mass almost equally except the small difference due to molecular diffusion. (*b*) Different initial and boundary conditions for active heat and passive mass (present study): passive mass is less affected by buoyancy because of the weak correlation between active heat and passive mass.

dimensionless time, $Nt(= Nx/U_{av})$, together with the measurements (Runs E-II and E-III). The computational results in figures 22 and 23 are in good qualitative agreement with the measurements despite the assumption of the same molecular diffusivity in the DNS for active heat and passive mass. This means that the large difference in eddy diffusivities between active heat and passive mass in stable stratification is not caused by the effects of the molecular diffusion but by the stable stratification.

The line in figure 23 is the prediction of K_H/K_S by Warhaft's model (Warhaft 1976), which was based on the second-order closure model. Although the measurements and DNS confirm the trend of the modelling, the model underpredicts the effect of stable stratification. This means that the models of the pressure strain terms in the active and passive scalar flux equations should be improved since the pressure strain terms in the transport equation are described by the active and passive scalar fluxes (Warhaft 1976).

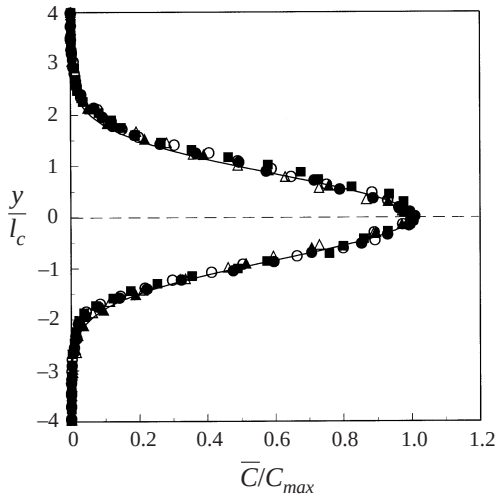

FIGURE 15. Vertical distributions of the normalized mean concentration in a plume in the neutrally stratified flow (by the DNS): ▲, $x/M = 10$; △, $x/M = 12$; ●, $x/M = 14$; ○, $x/M = 16$; ■, $x/M = 18$. The solid line shows the Gaussian curve (4.1).

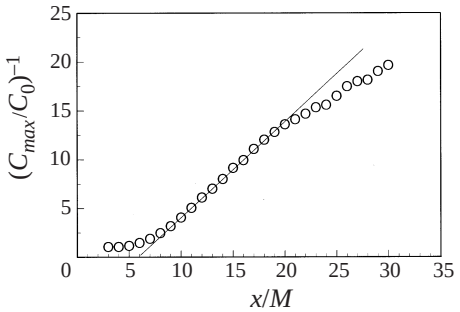

FIGURE 16. Streamwise variation of the reciprocal of the mean concentration on the plume axis (by the DNS).

5.3. *The evolution of the cospectra for active heat and passive mass fluxes*

To comprehend the difference in turbulent diffusion between active and passive scalars in the frequency domain, the cospectra for the active heat and passive mass fluxes, $Cs_{v\theta}$ and Cs_{vc},

$$\overline{v\theta} = \int_0^\infty Cs_{v\theta}(f)\,\mathrm{d}f, \qquad \overline{vc} = \int_0^\infty Cs_{vc}(f)\,\mathrm{d}f, \tag{5.1}$$

were computed by the DNS. Figure 24 shows the cospectra for the active heat and passive mass fluxes at $x/M = 10$, 14 and 18 in the strongly stratified water flow (Run S-III). Here the cospectra at the vertical location $y/M = -0.2$ are shown, since $\overline{vc} = 0$ and $\mathrm{d}\bar{C}/\mathrm{d}y = 0$ at $y/M = 0$. At the vertical location shown, negative and positive values of $Cs_{v\theta}$ and Cs_{vc} correspond to down- and counter-gradient heat and mass transfer, respectively. At $x/M = 10$ (figure 24*a*), both $Cs_{v\theta}$ and Cs_{vc} are negative in the whole frequency range. The negative cospectra show that at all scales the down-gradient heat and mass transfer is dominant. The cospectrum for the heat flux at $x/M = 14$ (figure 24*b*) changes its sign in the higher frequency range, showing counter-gradient heat transfer at small scales (Komori & Nagata 1996). However, the

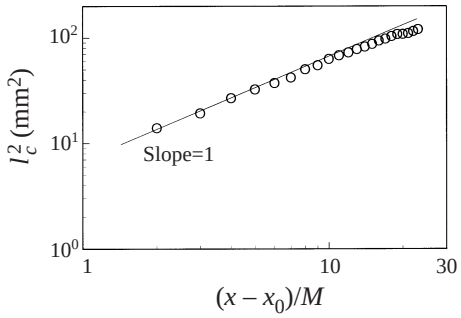

FIGURE 17. Streamwise variation of the square of the half-width of the mean concentration profile (by the DNS).

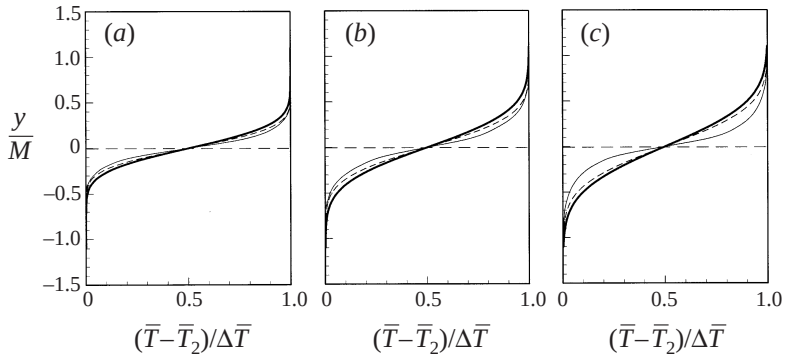

FIGURE 18. Vertical distributions of the mean temperature at (*a*) $x/M = 10$, (*b*) $x/M = 14$ and (*c*) $x/M = 18$ (by the DNS): ——, in the neutrally stratified flow (Run S-I); – – –, in the weakly stratified flow (Run S-II); ——, in the strongly stratified flow (Run S-III).

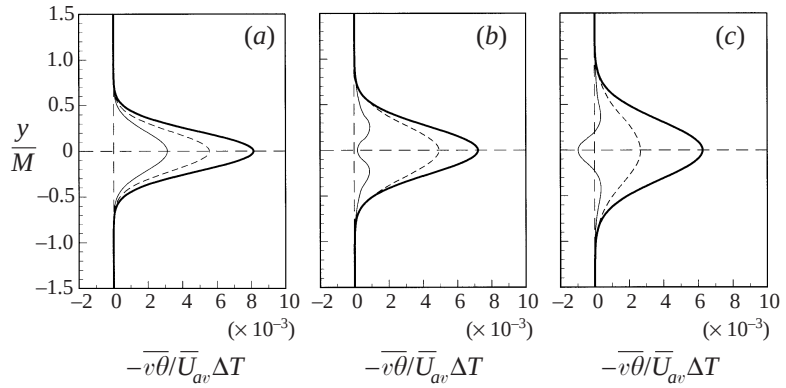

FIGURE 19. Vertical distributions of the normalized vertical heat flux at (*a*) $x/M = 10$, (*b*) $x/M = 14$ and (*c*) $x/M = 18$ (by the DNS). Lines as in figure 18.

cospectrum for the passive mass flux, Cs_{vc}, at the same location is still negative in the whole frequency range. At $x/M = 18$ (figure 24*c*), $Cs_{v\theta}$ becomes positive in the whole frequency range, while Cs_{vc} becomes positive only in the higher frequency range. The results show that the turbulent diffusion of passive scalar is less affected by buoyancy than that of active scalar.

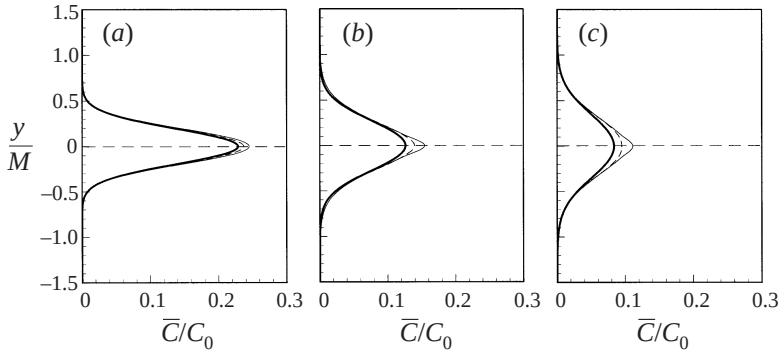

FIGURE 20. Vertical distributions of the mean concentration in a plume at (*a*) $x/M = 10$, (*b*) $x/M = 14$ and (*c*) $x/M = 18$ (by the DNS). Lines as in figure 18.

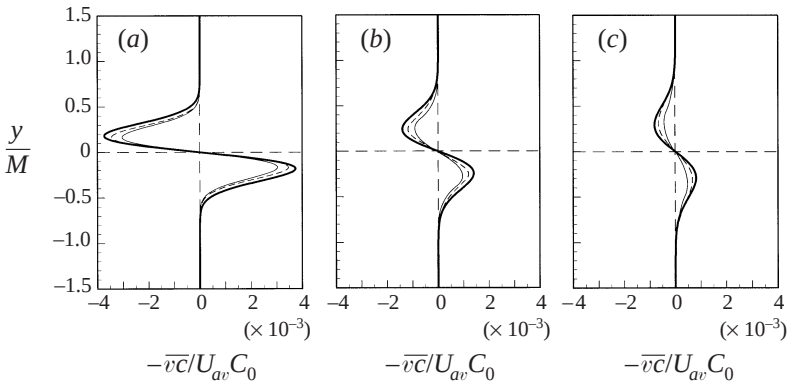

FIGURE 21. Vertical distributions of the normalized vertical mass flux at (*a*) $x/M = 10$, (*b*) $x/M = 14$ and (*c*) $x/M = 18$ (by the DNS). Lines as in figure 18.

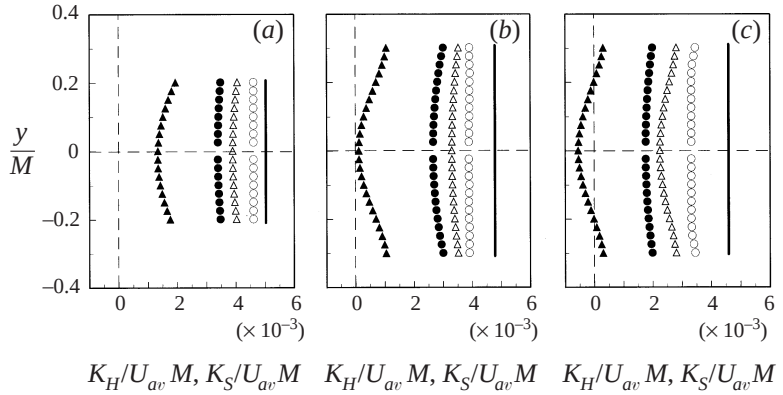

FIGURE 22. Vertical distributions of the eddy diffusivities for active heat and passive mass at (*a*) $x/M = 10$, (*b*) $x/M = 14$ and (*c*) $x/M = 18$ (by the DNS): ——, K_H and K_S in the neutrally stratified flow (Run S-I); △, K_H in the weakly stratified flow (Run S-II); ○, K_S in the weakly stratified flow (Run S-II); ▲, K_H in the strongly stratified flow (Run S-III); ●, K_S in the strongly stratified flow (Run S-III).

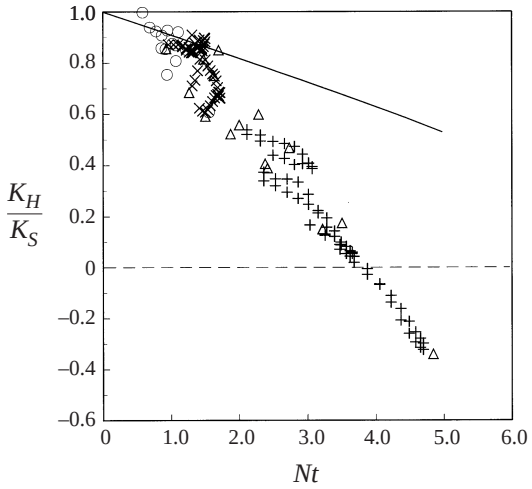

FIGURE 23. Time variations of the ratio of the eddy diffusivity for active heat to that for passive mass; ○, in the weakly stratified flow (from the experiment, Run E-II); △, in the strongly stratified flow (from the experiment, Run E-III); □, in the neutrally stratified flow (from the DNS, Run S-I); ×, in the weakly stratified flow (from the DNS, Run S-II); +, in the strongly stratified flow (from the DNS, Run S-III). The line shows the prediction by the second-order closure model (Warhaft 1976).

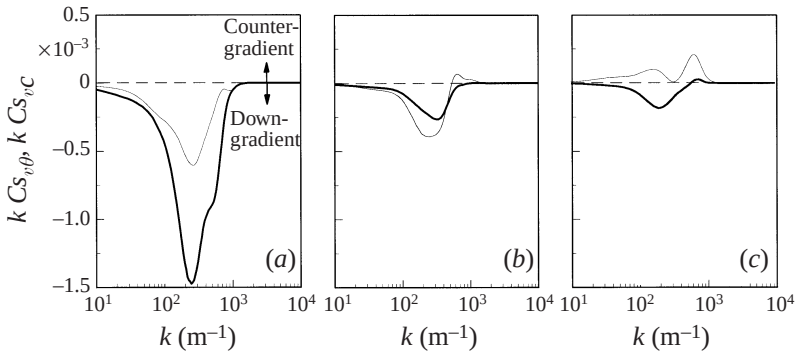

FIGURE 24. Cospectra for the active heat and passive mass fluxes in the strongly stratified water flow (Run S-III) at (*a*) $x/M = 10$ and $y/M = -0.2$, (*b*) $x/M = 14$ and $y/M = -0.2$ and (*c*) $x/M = 18$ and $y/M = -0.2$ (by the DNS): ——, $Cs_{v\theta}$; ——, Cs_{vc}. The cospectra are normalized by $U_{av}\Delta\bar{T}$ or $U_{av}C_0$.

5.4. *Difference in the eddy diffusivities in stratified air flows*

Figure 25 shows the ratio of the eddy diffusivity for active heat to that for passive mass against Nt in the neutrally (Run S-IV) and strongly stratified (Run S-V) air flows. The results show clear evidence of the difference in the eddy diffusivities. The ratio also decreases with increasing stability in stratified air flows as in stratified water flows.

The above DNS, together with the measurements in § 4, suggest that the assumption of the identical eddy diffusivity for active heat and passive mass, used in conventional turbulence models, gives significant errors in estimating turbulent diffusion of passive mass under stably stratified conditions.

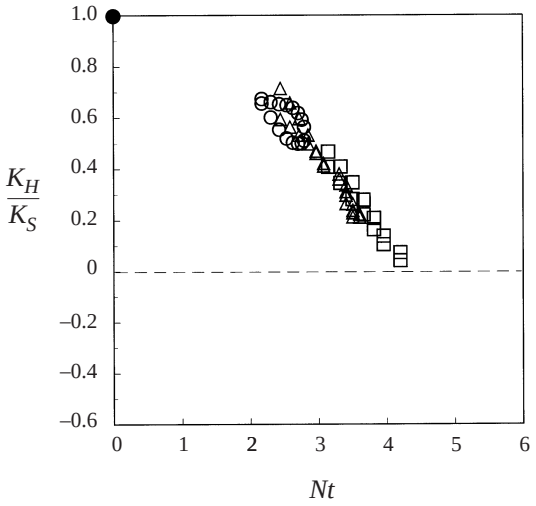

FIGURE 25. The ratio of the eddy diffusivity for active heat to that for passive mass in the strongly stratified air flow (Run S-V) as a function of Nt (by the DNS); ○, $x/M = 10$; △, $x/M = 14$; □, $x/M = 18$. The solid circle (●) shows the neutrally stratified case (Run S-IV).

6. Conclusions

The difference in turbulent diffusion between active scalar (heat) and passive scalar (mass) in stable thermal stratification was both experimentally and numerically investigated.

The main results from this study can be summarized as follows.

(*a*) Turbulent diffusion of passive scalar is less affected by buoyancy than that of active scalar when the initial and boundary conditions for active and passive scalars are not identical. The difference is attributed to the weak concentration–temperature correlation between active and passive scalars.

(*b*) For different initial and boundary conditions for active heat and passive mass, a stable stratification causes a large difference in the eddy diffusivities between active heat and passive mass. The difference suggests that the assumption of identical eddy diffusivity for active heat and passive mass, used in conventional turbulence models, gives significant errors in estimating turbulent diffusion of heat and mass in a stably thermally stratified flow.

The authors would like to thank Messrs H. Horibe and T. Iwabe for their help in conducting experiments. The direct numerical simulations were carried out by using a parallel super computer SX-4 of the Center for Global Environment Research, National Institute for Environmental Studies, Environmental Agency of Japan. This work was supported by the Japanese Ministry of Education, Science and Culture through grants-in-aid (Nos. 11450077 and 11750165).

REFERENCES

BRITTER, R. E., HUNT, J. C. R., MARSH, G. L. & SNYDER, W. H. 1983 The effects of stable stratification on turbulent diffusion and the decay of grid turbulence. *J. Fluid Mech.* **127**, 27–44.

CHAUDHRY, F. H. & MERONEY, R. N. 1973 A laboratory study of diffusion in stably stratified flow. *Atmos. Environ.* **7**, 443–454.

Freeman, B. E. 1977 Tensor diffusivity of a trace constituent in a stratified boundary layer. *J. Atmos. Sci.* **34**, 124–136.

Gad-el-Hak, M. & Morton, J. B. 1979 Experiments on the diffusion of smoke in isotropic turbulent flow. *AIAA J.* **17**, 558–562.

Gerz, T., Schumann, U. & Elghobashi, S. E. 1989 Direct numerical simulation of stratified homogeneous turbulent shear flows. *J. Fluid Mech.* **200**, 563–594.

Holt, S. E., Koseff, J. R. & Ferziger, J. H. 1992 A numerical study of the evolution and structure of homogeneous stably stratified sheared turbulence. *J. Fluid Mech.* **237**, 499–539.

Hunt, J. C. R. 1985 Diffusion in the stably stratified atmospheric boundary layer. *J. Climate Appl. Met.* **24**, 1187–1195.

Huq, P. & Britter, R. E. 1995 Turbulence evolution and mixing in a two-layer stably stratified sluid. *J. Fluid Mech.* **285**, 41–67.

Jacobitz, F. G., Sarkar, S. & Van Atta, C. W. 1997 Direct numerical simulations of the turbulence evolution in a uniformly sheared and stably stratified flow. *J. Fluid Mech.* **342**, 231–261.

Jayesh, Yoon, K. & Warhaft, Z. 1991 Turbulent mixing and transport in a thermally stratified interfacial layer in decaying grid turbulence. *Phys. Fluids* A **3**, 1143–1155.

Kaltenbach, H.-J., Gerz, T. & Schumann, U. 1994 Large-eddy simulation of homogeneous turbulence and diffusion in stably stratified shear flow. *J. Fluid Mech.* **280**, 1–40.

Komori, S. 1996 Turbulence structure and CO_2 transfer at the air-sea interface and turbulent diffusion in thermally-stratified flows. *CGER's Supercomputer Monograph Report, Vol. 1, CGER-I021-'96.* Center for Global Environment Research, National Institute for Environmental Studies, Environmental Agency of Japan.

Komori, S., Nagaosa, R., Murakami, Y., Chiba, S., Ishii, K. & Kuwahara, K. 1993*a* Direct numerical simulation of three-dimensional open-channel flow with zero-shear gas-liquid interface. *Phys. Fluids* A **5**, 115–125.

Komori, S. & Nagata, K. 1996 Effects of molecular diffusivities on counter-gradient scalar and momentum transfer in strongly stable stratification. *J. Fluid Mech.* **324**, 205–237.

Komori, S., Nagata, K., Kanzaki, T. & Murakami, Y. 1993*b* Measurements of mass flux in a turbulent liquid flow with a chemical reaction. *AIChE J.* **39**, 1611–1620.

Komori, S., Ueda, H., Ogino, F. & Mizushina T. 1983 Turbulence structure in stably stratified open-channel flow. *J. Fluid Mech.* **130**, 13–26.

Nagata, K. & Komori, S. 1996 Direct numerical simulation of the Prandtl number effect on the counter-gradient scalar transfer in strong stable stratification. *Trans. JSME* B (in Japanese) **62**, 3142–3148.

Nagata, K. & Komori, S. 2000 The effects of unstable stratification and mean shear on the chemical reaction in grid turbulence. *J. Fluid Mech.* **408**, 39–52.

Nakamura, I., Sakai, Y. & Miyata, M. 1987 Diffusion of matter by a non-buoyant plume in grid-generated turbulence. *J. Fluid Mech.* **178**, 379–403.

Pearson, H. J., Puttock, J. S. & Hunt, J. C. R. 1983 A statistical model of fluid-element motions and vertical diffusion in a homogeneous stratified turbulent flow. *J. Fluid Mech.* **129**, 219–249.

Rai, M. M. & Moin, P. 1991 Direct simulations of turbulent flow using finite-difference schemes. *J. Comput. Phys.* **96**, 15–53.

Warhaft, Z. 1976 Heat and moisture flux in the stratified boundary layer. *Q. J. R. Met. Soc.* **102**, 703–707.

Wyngaard, J. C., Coté, O. R. & Izumi, Y. 1971 Local free convection, similarity, and the budgets of shear stress and heat flux. *J. Atmos. Sci.* **28**, 1171–1182.

Yamada, T. & Mellor, G. 1975 A simulation of the Wangara atmospheric boundary layer data. *J. Atmos. Sci.* **32**, 2309–2329.